

**This item is the archived peer-reviewed author-version of:**

Room temperature magnetically ordered polar corundum  $GaFeO_3$  displaying magnetoelectric coupling

**Reference:**

Niu Hongjun, Pitcher Michael J., Corkett Alex J., Ling Sanliang, Mandal Pranab, Zanella Marco, Dawson Carl, Stamenov Plamen, Batuk Dmitry, Abakumov Artem M., ....-  
Room temperature magnetically ordered polar corundum  $GaFeO_3$  displaying magnetoelectric coupling  
Journal of the American Chemical Society / American Chemical Society - ISSN 0002-7863 - 139:4(2017), p. 1520-1531  
Full text (Publisher's DOI): <https://doi.org/10.1021/JACS.6B11128>  
To cite this reference: <https://hdl.handle.net/10067/1475070151162165141>

1  
2  
3 **Room temperature magnetically ordered polar corundum GaFeO<sub>3</sub> displaying**  
4 **magnetoelectric coupling**  
5

6 Hongjun Niu<sup>1</sup>, Michael J. Pitcher<sup>1</sup>, Alex J. Corkett<sup>1</sup>, Sanliang Ling<sup>2</sup>, Pranab Mandal<sup>1</sup>, Marco  
7 Zanella<sup>1</sup>, Karl Dawson<sup>3</sup>, Plamen Stamenov<sup>4</sup>, Dmitry Batuk<sup>5</sup>, Artem M. Abakumov<sup>5,6</sup>, Craig  
8 L. Bull<sup>7</sup>, Ronald I. Smith<sup>7</sup>, Claire A. Murray<sup>8</sup>, Sarah J. Day<sup>8</sup>, Ben Slater<sup>2</sup>, Furio Cora<sup>2</sup>, John  
9 B. Claridge<sup>1,\*</sup> and Matthew J. Rosseinsky<sup>1,\*</sup>  
10  
11

12  
13  
14 <sup>1</sup>Department of Chemistry, University of Liverpool, Crown Street, Liverpool L69 7ZD, UK  
15

16 <sup>2</sup>Department of Chemistry, University College London, Gower Street, London WC1E 6BT,  
17 UK  
18

19  
20 <sup>3</sup>Centre for Materials and Structures, School of Engineering, University of Liverpool,  
21 Liverpool L69 3GH, UK  
22

23  
24 <sup>4</sup>CRANN, Trinity College Dublin, College Green, Dublin 2, Republic of Ireland  
25

26  
27 <sup>5</sup>EMAT, University of Antwerp, Groenenborgerlaan 171, 2020 Antwerp, Belgium  
28

29  
30 <sup>6</sup>Skoltech Center for Electrochemical Energy Storage, Skolkovo Institute of Science and  
31 Technology, 143026 Moscow, Russian Federation  
32

33  
34 <sup>7</sup>ISIS Neutron and Muon Source, Science and Technology Facilities Council, Rutherford  
35 Appleton Laboratory, Harwell Oxford, Didcot, Oxfordshire OX11 0QX, UK  
36

37  
38 <sup>8</sup>Diamond Light Source, Diamond House, Harwell Oxford, Didcot, Oxfordshire OX11 0DE,  
39 UK  
40

41  
42 **Abstract**  
43

44 The polar corundum structure type offers a route to new room temperature multiferroic  
45 materials, as the partial LiNbO<sub>3</sub>-type cation ordering that breaks inversion symmetry may be  
46 combined with long range magnetic ordering of high spin *d<sup>5</sup>* cations above room temperature  
47 in the AFeO<sub>3</sub> system. We report the synthesis of a polar corundum GaFeO<sub>3</sub> by a high-pressure  
48 high-temperature route and demonstrate that its polarity arises from partial LiNbO<sub>3</sub>-type  
49 cation ordering by complementary use of neutron, X-ray and electron diffraction methods. In-  
50 situ neutron diffraction shows that the polar corundum forms directly from AlFeO<sub>3</sub>-type  
51 GaFeO<sub>3</sub> under the synthesis conditions. The A<sup>3+</sup>/Fe<sup>3+</sup> cations are shown to be more ordered in  
52 polar corundum GaFeO<sub>3</sub> than in isostructural ScFeO<sub>3</sub>. This is explained by DFT calculations  
53  
54  
55  
56  
57  
58  
59  
60

1  
2  
3 that indicate that the extent of ordering is dependent on the configurational entropy available  
4 to each system at the very different synthesis temperatures required to form their corundum  
5 structures. Polar corundum GaFeO<sub>3</sub> exhibits weak ferromagnetism at room temperature that  
6 arises from its Fe<sub>2</sub>O<sub>3</sub>-like magnetic ordering, which persists to a temperature of 408 K. We  
7 demonstrate that the polarity and magnetisation are coupled in this system, with a measured  
8 linear magnetoelectric coupling coefficient of 0.057 ps/m. Such coupling is a prerequisite for  
9 potential applications of polar corundum materials in multiferroic/magnetoelectric devices.  
10  
11  
12  
13  
14  
15  
16  
17

## 18 **1. Introduction**

19  
20 New low-energy information storage and processing architectures have been proposed which  
21 rely on magnetoelectric and multiferroic materials<sup>1-2</sup>, but the development of such systems is  
22 hampered by a paucity of suitable candidate materials, which must combine magnetic and  
23 polar electrical order at (or close to) room temperature. This is challenging because the  
24 electronic structure requirements for the two ground states are antagonistic in several respects  
25 *e.g.*, classical routes to polar materials rely on the coordination environments of closed shell  
26 *s*<sup>2</sup> and *d*<sup>0</sup> cations which are not consistent with magnetism<sup>3-5</sup>. The perovskite BiFeO<sub>3</sub> partially  
27 solves this problem by combining ferroelectrically- and antiferromagnetically-ordered  
28 sublattices<sup>6-7</sup>. Several new approaches centred on the ABO<sub>3</sub> perovskite family have emerged  
29 recently, such as strain-generated ferromagnetism in epitaxial thin films<sup>8-9</sup>, magnetic  
30 percolation at morphotropic phase boundary compositions in bulk ceramics<sup>10</sup> and symmetry  
31 engineering<sup>11</sup> in bulk<sup>12</sup> and thin film materials<sup>13</sup>. However, the identification of other  
32 materials families where the two ground states may co-exist at ambient temperature is less  
33 developed. By using the connection between the polar LiNbO<sub>3</sub> structure and perovskite, we  
34 identified polar derivatives of corundum as a new class of ternary oxide AFeO<sub>3</sub> materials that  
35 support both magnetic order (from a sufficiently high concentration of Fe<sup>3+</sup> cations) and  
36 electrical order (enabled by cation site ordering), which can be targeted by high pressure  
37 synthesis methods<sup>14</sup>. The polar corundum ScFeO<sub>3</sub>, the first compound of this type, is ordered  
38 magnetically above room temperature and the limited extent of long-range cation site order is  
39 sufficient to break inversion symmetry, producing electrical polarity (more recently, LiNbO<sub>3</sub>-  
40 type polymorphs of Mn<sub>2</sub>FeTaO<sub>6</sub><sup>15</sup> and Zn<sub>2</sub>FeTaO<sub>6</sub><sup>16</sup> have been reported with low magnetic  
41 ordering temperatures by a similar synthetic approach, and potential ferroelectric switching  
42 mechanisms have been investigated computationally<sup>17</sup>). The crystal chemistry of ScFeO<sub>3</sub> is  
43  
44  
45  
46  
47  
48  
49  
50  
51  
52  
53  
54  
55  
56  
57  
58  
59  
60

1  
2  
3 complex as, in addition to the competition between bixbyite and partially ordered corundum  
4 phases,<sup>14</sup> higher synthesis pressures stabilise a perovskite phase, from which a fully ordered  
5 LiNbO<sub>3</sub>-type polymorph (with a correspondingly enhanced spontaneous polarisation and  
6 Néel temperature) is recovered on decompression<sup>18</sup>. This implies that the structural chemistry  
7 of analogous *A*FeO<sub>3</sub> compositions (where *A* is a trivalent cation capable of adopting  
8 octahedral coordination) could offer polarity and magnetism if synthesised under appropriate  
9 conditions.  
10

11  
12  
13  
14  
15 The ternary ferrite GaFeO<sub>3</sub> represents one such candidate for isolation of a polar corundum  
16 phase. While at ambient pressure ScFeO<sub>3</sub> adopts the fluorite-derived bixbyite structure with  
17 Sc<sup>3+</sup> and Fe<sup>3+</sup> coordinated in an edge-sharing network of distorted MO<sub>6</sub> octahedra<sup>19</sup>, ambient  
18 pressure GaFeO<sub>3</sub> adopts the polar orthorhombic AlFeO<sub>3</sub> structure with edge-sharing chains of  
19 (Ga, Fe)O<sub>6</sub> octahedra and vertex-linked GaO<sub>4</sub> tetrahedra, but only exhibits long-range  
20 magnetic ordering and magnetoelectric coupling well below room temperature<sup>20-23</sup>. Like  
21 ScFeO<sub>3</sub> and InFeO<sub>3</sub><sup>24</sup>, its structural behaviour at high pressures and temperatures shows  
22 complex interplay between corundum and perovskite structures: at ambient temperature,  
23 hydrostatic compression to pressures above 40 GPa converts the structure directly to an  
24 orthorhombic perovskite, which in turn transforms on decompression to 25 GPa to a  
25 corundum-type phase which is retained down to ambient pressure<sup>25</sup>. Corundum-type GaFeO<sub>3</sub>  
26 can also be obtained directly by annealing at a sufficiently high temperature and pressure<sup>26</sup>  
27 and by analogy with ScFeO<sub>3</sub> it is possible that a polar variant of this structure will be  
28 accessible in this part of the phase diagram. We have targeted and isolated such a polar  
29 corundum GaFeO<sub>3</sub> phase, demonstrating that a family of materials adopt this structure. Polar  
30 corundum GaFeO<sub>3</sub> exhibits weak ferromagnetism above room temperature, and the extent of  
31 the cation site order is enhanced with respect to that observed in ScFeO<sub>3</sub>, allowing the  
32 measurement of linear magnetoelectric coupling consistent with the polar *R3c* space  
33 symmetry and the observed  $\alpha$ -Fe<sub>2</sub>O<sub>3</sub> – like magnetic order.  
34  
35  
36  
37  
38  
39  
40  
41  
42  
43  
44  
45  
46  
47  
48  
49

## 50 2. Experimental Details

51  
52 **Synthesis:** Initially, the ambient pressure phase of GaFeO<sub>3</sub> was prepared from stoichiometric  
53 mixtures of Ga<sub>2</sub>O<sub>3</sub> (99.999%) and Fe<sub>2</sub>O<sub>3</sub> (99.998%) reacted at 900 °C for 12 hours, 1300 °C  
54 for 24 hours followed by 1400 °C for 2 hours in an alumina crucible in air. This precursor  
55 phase was then annealed under flowing oxygen at 1300 °C for 10 hours, in order to maximise  
56  
57  
58  
59  
60

1  
2  
3 the resistivity of the subsequent high pressure product. The GaFeO<sub>3</sub> starting materials were  
4 then heated to 150, 500, 700, 900, 1100, 1300 and 1500 °C, respectively, for 10 minutes at 6  
5 GPa in a Pt-lined alumina crucible encapsulated within a graphite furnace in a Walker-type  
6 multi-anvil press. The samples were then cooled to room temperature and the pressure  
7 released. The high pressure phase forming at 900 °C was used for structural, electric and  
8 magnetic studies.

9  
10 **Powder X-ray diffraction:** Phase identification was performed using a PANalytical X'Pert  
11 Pro diffractometer in Bragg-Brentano geometry with monochromated Co K<sub>α1</sub> radiation ( $\lambda =$   
12  $1.78896 \text{ \AA}$ ). Synchrotron XRD data (SXRD) were collected from the I11 powder  
13 diffractometer (Diamond Light Source, UK). The sample was loaded inside a 0.1 mm quartz  
14 capillary and data were collected using an incident wavelength  $\lambda = 0.827127(1) \text{ \AA}$  over a  $2\theta$   
15 range  $2 - 150^\circ$ , using the high resolution MAC detectors. Anomalous scattering data were  
16 collected on beam line I11 from a sample loaded on to the external surface of a 0.3 mm  
17 borosilicate capillary. A monochromator scan was used to measure the Ga K edge  
18 fluorescence spectrum and an energy of 10.359 keV ( $\lambda = 1.196901(5) \text{ \AA}$ ) was selected for the  
19 anomalous scattering data set using the high resolution MAC detectors. A corresponding non-  
20 anomalous data set was then collected from the same capillary at  $\lambda = 0.826185(5) \text{ \AA}$ .

21  
22 **Powder neutron diffraction:** Time-of-flight neutron powder diffraction (NPD) data were  
23 collected at ambient temperature and pressure on the POLARIS diffractometer at the ISIS  
24 facility, Rutherford Appleton Laboratory (UK). The sample was contained in a quartz  
25 capillary of diameter 1.5 mm, filled to a height of 40 mm. The data analysis was performed  
26 by Rietveld refinement using Topas Academic (Version 5).

27  
28 **In-situ powder neutron diffraction:** High-pressure high-temperature data were collected on  
29 the medium-resolution high-flux PEARL diffractometer (ISIS, UK) using a Paris-Edinburgh  
30 (PE) press<sup>27</sup>. The sample was pelletised and placed in a high-pressure furnace assembly<sup>28</sup>.  
31 The furnace assembly was placed in between WC anvils in a V4 variant PE press dedicated to  
32 high temperature pressure measurements. The sample pressure was determined by the  
33 equation of state (EoS) of platinum<sup>29</sup>. The temperature was determined by the resonance  
34 technique from the Hf foils included in the sample volume<sup>30</sup>. Time of flight data were  
35 collected using the 90 degree detector bank over a d-spacing range of 0.5-4 Å and corrected  
36 for anvil attenuation using in-house routines<sup>27</sup>. The hydraulic load of the press was gradually  
37 increased until the desired sample pressure was achieved prior to heating. The data analysis  
38 was performed by Rietveld refinement using Topas Academic (Version 5).

1  
2  
3 **SQUID Magnetometry:** Magnetic measurements were carried out on powder samples using  
4 a commercial superconducting quantum interference device (SQUID) magnetometer MPMS  
5 XL – 7 and MPMS3 (Quantum Design, USA). Magnetization vs. temperature data were  
6 recorded from 5 K to 900 K in the following modes: ZFC (zero-field cooling), FC (field  
7 cooling) and TRM (thermoremanent magnetization). The magnetic field-dependent  
8 magnetization was also measured at 10, 200, 400 and 420 K between -9 kOe and 9 kOe.

9  
10  
11 **Magnetoelectric coupling:** For magnetoelectric (ME) measurements, the polar corundum  
12 sample was polished to a 5 micron finish using SiC paper in a semi-automatic polishing  
13 machine. Ohmic contacts were made via sputtering Pt. ME measurements were carried out on  
14 a modified SQUID magnetometer<sup>31</sup>. Prior to the measurements the sample was poled in the  
15 following sequence: slowly cooled (1 - 2 K/min) from 350 K to 130 K in a 20 kOe magnetic  
16 field and zero electric field (short circuit). At 100 K, an electric field of 350 – 400 kV/m was  
17 applied while cooling down in the same magnetic field to the measurement temperature at 1  
18 K/min. After poling, electric and magnetic fields were switched off and electrodes were short  
19 circuited for 15 minutes.

20  
21  
22 **Dielectric constant** Dielectric properties were measured using an Agilent 4980 precision  
23 LCR meter for frequencies of 20 Hz to 2 MHz in the temperature range of 30–500 °C. A  
24 ramp rate of 1 °C min<sup>-1</sup> was used. The sample with sputter coated Pt electrodes on both sides  
25 was loaded in a home-made sample holder and data were collected using the LABVIEW  
26 program.

27  
28  
29 **Differential Scanning Calorimetry (DSC):** Heat flow was measured from a powder sample  
30 in an aluminium pan between room temperature to 500 °C by the modulated DSC technique  
31 using a DSC Q2000 instrument (TA Instruments).

32  
33  
34 **In-situ resistance:** Two-probe dc electrical resistance measurements as a function of  
35 temperature at 6 GPa were carried out using Keithley 220 programmable current source and  
36 Keithley 2182 Nanovoltmeter. The GaFeO<sub>3</sub> powder was loaded into the alumina crucible and  
37 Pt plates were employed on both the top and bottom of the crucible as the electrodes.

38  
39  
40 **ICP-OES measurements:** Powder samples of GaFeO<sub>3</sub> (approximately 50 mg) were  
41 dissolved in 10 cm<sup>3</sup> HF-HCl mixture (UniSolv Acid Dissolution Reagent 1, Inorganic  
42 Ventures) with 10 drops of concentrated HNO<sub>3</sub>. The solution was then neutralised with 50  
43 cm<sup>3</sup> of triethanolamine-triethylenetetramine solution (UNS-1 solution, Inorganic Ventures)  
44 and diluted to approximately 20 ppm. The same protocol was used to prepare a standard  
45 solution from a stoichiometric mixture of Ga<sub>2</sub>O<sub>3</sub> and Fe<sub>2</sub>O<sub>3</sub>. Measurements were collected on  
46 a Spectro Ciros Vision ICP-OES instrument.

1  
2  
3 **TEM-EDX:** EDX measurements were performed on a Jeol 2000FX using an EDAX EDX  
4 detector. Sample powder was dispersed in 500 $\mu$ l of ethanol and a drop of the suspension was  
5 dropped on a carbon coated TEM copper grid. EDX spectra were collected for several  
6 minutes in order to obtain a suitable signal to noise ratio. Compositions were calculated from  
7 the mean of 25 particles.  
8  
9

10  
11 **Convergent beam electron diffraction (CBED):** Specimens were prepared using a FEI  
12 Helios 600i focussed (Ga) ion beam instrument. Thin lamellae were sectioned and mounted  
13 on Cu grids using the lift out technique. Primary milling was performed using an acceleration  
14 voltage of 30kV, final cleaning passes were applied to specimen surfaces using a low energy  
15 (5kV) polish. CBED experiments were performed in JEOL 2000FX microscope operated at  
16 200keV.  
17  
18

19  
20 **SAED and HAADF-STEM:** TEM specimens were prepared by grinding the powder sample  
21 under ethanol and depositing several drops of the dispersion onto holey carbon grids. The  
22 selected area electron diffraction (SAED) patterns were recorded using a Tecnai G2  
23 microscope operated at 200 kV. The Fe and Ga distribution in the structure was investigated  
24 using high angle annular dark field scanning TEM (HAADF-STEM) imaging. The  
25 experiment was conducted on a probe aberration-corrected Titan 80-300 microscope operated  
26 at 300 kV. Theoretical HAADF-STEM images have been calculated using the QSTEM 2.20  
27 software.  
28  
29

30  
31 **Mossbauer spectroscopy:** Mössbauer spectroscopy was performed in absorption, at room  
32 temperature, using a WissEl (MA-260) electromagnetic Doppler drive system, a  $^{57}\text{Co}(\text{Rh})$   
33 gamma source, of actual activity of  $\sim 40$  mCi and Xe-gas Reuter-Stokes proportional counter.  
34 Canberra amplification, discrimination and scaling electronics were used to acquire sample  
35 and  $\alpha$ -Fe calibration spectra of width of 512 channels, to a level of approximately  $10^7$  counts  
36 per channel. Samples were diluted with sucrose (icing sugar) for measurements at an  
37 approximate ratio of 0.2, in order to prevent excessive line-shape distortion and non-resonant  
38 absorption. Custom folding, absorber geometry modelling and non-linear least squares  
39 regression routines were used for the extraction of the spectroscopic parameters and their  
40 errors. Isomer shifts are referred to the source.  
41  
42

43  
44 **Computational:** All calculations were performed under periodic boundary conditions, using  
45 the CP2K<sup>32-33</sup> code which employs a mixed Gaussian/plane-wave basis set. We employed  
46 double- $\zeta$  polarization quality Gaussian basis sets<sup>34</sup> and a 600 Ry plane-wave cutoff for the  
47 auxiliary grid, in conjunction with Goedecker–Teter–Hutter pseudopotentials<sup>35-36</sup>. Total  
48 energy calculations and structural optimizations, including both atomic coordinates and cell  
49  
50  
51  
52  
53  
54  
55  
56  
57  
58  
59  
60

parameters, were performed at the hybrid density functional theory (DFT) level using the PBE0 exchange and correlation functional<sup>37-38</sup>, which has 25% Hartree-Fock exchange (HFX). The HFX calculations were significantly accelerated by using the auxiliary density matrix method (ADMM)<sup>39</sup> and a truncated potential<sup>40</sup>, with which the HFX energy becomes zero beyond a pre-defined real-space cutoff radius. For production quality calculations we have used the cpFIT3 auxiliary basis sets and a cutoff radius of 4 Å, a convergence threshold of  $5.0 \times 10^{-6}$  Ha for the self-consistent field cycle, and structural optimizations were considered to have converged when the maximum force on all atoms falls below  $4.5 \times 10^{-4}$  Ha Bohr<sup>-1</sup>. Calculations were performed with the  $\Gamma$ -point approximation using a  $2 \times 2 \times 1$  multiplication of the hexagonal primitive cell consisting of 120 atoms. Additional calculations in a  $3 \times 3 \times 1$  supercell (270 atoms) show that the relative energy between FM and AFM magnetic configurations in the LiNbO<sub>3</sub> cation order converged to within 5 meV/f.u. in the  $2 \times 2 \times 1$  supercell. A comprehensive and systematic configurational and compositional search on ScFeO<sub>3</sub> and GaFeO<sub>3</sub> in the corundum structure was performed as part of this study (described fully in the Supporting Information), in which the LiNbO<sub>3</sub> structure was identified as the ground state of corundum-type ScFeO<sub>3</sub>. The ground state of corundum-type GaFeO<sub>3</sub> was found to be phase separated layers of Fe<sub>2</sub>O<sub>3</sub> and Ga<sub>2</sub>O<sub>3</sub>, hence discussion of phase stability refers to LiNbO<sub>3</sub> and “phase separated” as the ground state references for ScFeO<sub>3</sub> and GaFeO<sub>3</sub> respectively. Additional details of the computational study, including defect formation energies, configurational search, and estimation of configurational entropies, are provided in the Supporting Information (including Figures S1 – S3, and Tables S1 – S2).

### 3. Results

#### 3.1. Isolation and stability of corundum GaFeO<sub>3</sub>

Extensive investigation of (T, P) synthesis conditions in the multianvil cell revealed a 700-900°C temperature range at 6 GPa that afforded a diffraction pattern that could be indexed solely with a corundum unit cell after decompression and cooling to room temperature (Figure 1a). The composition was confirmed to be stoichiometric GaFeO<sub>3</sub> by ICP-OES measurements (Table S3), with a high level of compositional homogeneity confirmed by TEM-EDX (Figure S4). Reaction at higher temperatures produces Fe<sub>3</sub>O<sub>4</sub> as a secondary phase in increasing quantity (2 wt.% 1100°C, 19 wt.% 1500°C) while 500 °C affords partial



1  
2  
3 conversion of ambient pressure GaFeO<sub>3</sub> to the corundum structure. In-situ neutron diffraction  
4 data collected at 4.7 GPa confirms that the ambient pressure orthorhombic GaFeO<sub>3</sub> is  
5 converted directly to a corundum-type phase (Figure 1b, c). Higher resolution information on  
6 the transformation temperature is provided by in-situ measurement of dc resistance under the  
7 synthesis conditions: by cycling a sample to increasing maximum temperatures, its resistance  
8 was found to decrease irreversibly during cycles to 400 and 550 °C signifying the onset of the  
9 phase transformation, before returning to near-reversible behaviour for cycles to 650 and 800  
10 °C, consistent with completed formation of the corundum phase (Figure 1d). A second  
11 sample was cycled four times between ~25 – 900 °C and showed an irreversible decrease in  
12 resistance on the first cycle, which coincides with the resistivity of subsequent cycles at 550  
13 °C (Figure S5), implying that complete conversion to the corundum is achieved at this  
14 temperature. This is consistent with both the ex-situ PXRD where the pattern is already  
15 dominated by the corundum phase at 500 °C, and the in-situ NPD where the refined AlFeO<sub>3</sub>-  
16 phase content reaches a minimum plateau at 575 °C.

17  
18 To better understand the isolation of polar corundum GaFeO<sub>3</sub> under high pressure reaction  
19 conditions, we calculated the enthalpies of different polymorphs of GaFeO<sub>3</sub> at different  
20 pressures up to 40 GPa. We considered the ambient pressure AlFeO<sub>3</sub>-type structure, an  
21 orthorhombic perovskite structure, the LiNbO<sub>3</sub> and ilmenite ordered corundum structures,  
22 and the ground state corundum configuration produced by our configurational search (in  
23 which Ga and Fe form a structure with distinct [001] blocks at either end of the corundum  
24 cell, see Supporting Information and Figure S1). Their enthalpies were compared with those  
25 of the binary oxides using the ambient pressure forms  $\alpha$ -Fe<sub>2</sub>O<sub>3</sub> and  $\beta$ -Ga<sub>2</sub>O<sub>3</sub> as the  
26 references. Finally, an estimate of the configurational entropies available to the AlFeO<sub>3</sub>- and  
27 LiNbO<sub>3</sub>-type structures was calculated at 1200 K (see Supplementary Text). The calculated  
28 enthalpies as a function of pressure are plotted in Figure 2a, with the estimated entropic  
29 contribution to the total energy at 1200 K overlaid for these two structure types to illustrate  
30 the estimated extent of entropic stabilization. The equivalent calculations for the same  
31 polymorphs of ScFeO<sub>3</sub>, using  $\alpha$ -Fe<sub>2</sub>O<sub>3</sub> and bixbyite-type Sc<sub>2</sub>O<sub>3</sub> as the references, are shown  
32 in Figure 2b.

33  
34 For GaFeO<sub>3</sub>, the ambient pressure AlFeO<sub>3</sub> structure is the most stable ternary phase at 0 GPa,  
35 and is stable relative to the binaries when configurational entropy of 98.8 meV/f.u. at 1200 K  
36 is considered. At this pressure, the LiNbO<sub>3</sub> structure is unstable with respect to its binary  
37 constituents by 159 meV/f.u at 0 K. With increasing pressure, the AlFeO<sub>3</sub> structure is  
38  
39  
40  
41  
42  
43  
44  
45  
46  
47  
48  
49  
50  
51  
52  
53  
54  
55  
56  
57  
58  
59  
60

1  
2  
3 progressively destabilised, and the corundum-type structures become the most stable beyond  
4  $\sim 3$  GPa. Among the corundum-type structures, the LiNbO<sub>3</sub> cation ordering is found to be  
5 more stable than the ilmenite ordering at all pressures. At  $\sim 30$  GPa the perovskite structure  
6 becomes more stable than the LiNbO<sub>3</sub> structure, which is in good agreement with  
7 experimental work<sup>25</sup>. In ScFeO<sub>3</sub>, the LiNbO<sub>3</sub> structure is the most stable ternary phase at 0  
8 GPa but is less stable than the binary mixture by 128 meV/f.u.; the orthorhombic perovskite  
9 phase is stabilised more rapidly with pressure and becomes the most enthalpically stable  
10 phase at  $\sim 7$  GPa.

11 These results show that configurational entropy due to disorder of Ga and Fe cations in the  
12 AlFeO<sub>3</sub> and corundum lattices at the synthesis temperatures plays a critical role in the  
13 stabilisation of the ternary phases. This is consistent with our configurational search of  
14 corundum-type GaFeO<sub>3</sub> (see Figure 3a), where a total of 151 configurations, including the  
15 fully ordered LiNbO<sub>3</sub> structure, are found within 50 meV/f.u. ( $\sim 0.5$   $kT$  at the synthesis  
16 temperature of 1200 K) of the lowest energy configuration: these may correspond to states  
17 that are accessible under the synthesis temperature. This contrasts with ScFeO<sub>3</sub>, which has  
18 only 5 configurations within 50 meV/f.u. of the fully ordered LiNbO<sub>3</sub> ground state (Figure  
19 3b), indicating that a higher temperature is required to entropically stabilise the corundum  
20 structure of ScFeO<sub>3</sub> by accessing a greater number of configurations.

### 3.2. Structural analysis

21 The synchrotron powder X-ray diffraction (SXRD) patterns of GaFeO<sub>3</sub> synthesised at high  
22 pressure could be indexed to an  $R$ -centered hexagonal unit cell with lattice parameters  $a =$   
23  $5.01936(4)$  Å,  $c = 13.5903(1)$  Å), as shown in Figure 4a, which is consistent with the  
24 corundum structure adopted by  $\alpha$ -Fe<sub>2</sub>O<sub>3</sub><sup>41-42</sup>. The observed reflection conditions ( $h$ - $h$ 0 $l$ :  $h+l =$   
25  $3n$ ,  $l = 2n$ ), also observed in selected area electron diffraction (SAED) patterns (Figure 4c),  
26 are consistent with  $R3c$  and  $R\bar{3}c$  space groups which correspond to the polar LiNbO<sub>3</sub> and  
27 non-polar (fully disordered) corundum structures respectively. These systematic absences  
28 preclude the possibility of an ilmenite structure type with  $R\bar{3}$  space symmetry. Regarding the  
29 possible acentric  $R3c$  and centrosymmetric  $R\bar{3}c$  structural models of GaFeO<sub>3</sub>, the very similar  
30 X-ray scattering factors of Fe<sup>3+</sup> and Ga<sup>3+</sup> preclude unambiguous space group assignment  
31 from Rietveld refinement against PXRD data alone. We addressed this problem in two parts:  
32 firstly, by using convergent beam electron diffraction (CBED) to determine the point group  
33  
34  
35  
36  
37  
38  
39  
40  
41  
42  
43  
44  
45  
46  
47  
48  
49  
50  
51  
52  
53  
54  
55  
56  
57  
58  
59  
60

of the GaFeO<sub>3</sub> corundum; and secondly by employing powder neutron diffraction and anomalous X-ray scattering to determine the extent of the cation ordering.

The whole pattern symmetry of the [5 $\bar{5}$ 1] zone from CBED (Figure 4b) displays only a single *m* symmetry element. Considering only trigonal crystal systems this permits the assignment of the *3m* point group<sup>43</sup> and along with the observed reflection conditions from PXRD data indicates that the high pressure phase of GaFeO<sub>3</sub> crystallises in the non-centrosymmetric *R3c* space group. To confirm the assignment of the *R3c* space group and investigate the degree of cation order in GaFeO<sub>3</sub>, neutron powder diffraction (NPD) analysis of two samples synthesised by the same protocol utilized the modest contrast in the neutron scattering lengths of Fe (9.45 fm) and Ga (7.288 fm). The appearance of Bragg peaks that were not present in the SXRD pattern, including two intense reflections at 4.14 and 4.54 Å, confirmed the presence of long range magnetic order at room temperature. The magnetic structure was determined by representational analysis using the SARAh package<sup>44</sup> and found to be a *k* = 0 G-type antiferromagnetic arrangement analogous to the high temperature antiferromagnetic structure of  $\alpha$ -Fe<sub>2</sub>O<sub>3</sub><sup>45</sup> with spins aligned parallel to the *a* axis. Structural models in *R3c* (LiNbO<sub>3</sub>) and  $R\bar{3}c$  (corundum) were refined against four Polaris data banks simultaneously, with the magnetic structure modelled in a *P1* cell. In the disordered corundum ( $R\bar{3}c$ ) refinement, the magnitudes of the magnetic moments were constrained to a single refined value to reflect the statistical distribution of Fe<sup>3+</sup> cations. In the cation-ordered model (*R3c*), the occupancies of Ga<sup>3+</sup> and Fe<sup>3+</sup> on each site in the nuclear phase were refined with a constraint on the total composition, and the magnetic phases were modelled with two independently refined moments, whose positions in the *P1* cell corresponded to the LiNbO<sub>3</sub>-type cation ordering. In addition to site occupancy refinement in the LiNbO<sub>3</sub> model, atomic coordinates and isotropic thermal displacement parameters (*B*<sub>iso</sub>) were refined with *B*<sub>iso</sub> constrained to be equal for the Fe/Ga sites.

For both samples the best goodness of fit was obtained from refinement in the *R3c* space group, with  $R\bar{3}c$  (disordered corundum) giving the higher  $\chi^2$  (see Tables S4 and S5). Inspection of the refined *R3c* model revealed that the refined cation occupancies from the nuclear scattering in *R3c* resulted in compositions of [Ga<sub>0.68(2)</sub>Fe<sub>0.32(2)</sub>][Ga<sub>0.32(2)</sub>Fe<sub>0.68(2)</sub>]O<sub>3</sub> (36(2) % ordered, defined by the difference in site occupancy) and [Ga<sub>0.62(3)</sub>Fe<sub>0.38(3)</sub>][Ga<sub>0.38(3)</sub>Fe<sub>0.62(3)</sub>]O<sub>3</sub> (24(3)% ordered) for the two samples, which is consistent with the relative magnitudes of the ordered spins on each site in the magnetic structure: the ordered moment at the Fe-rich site in sample 1 refined to 2.15(2)  $\mu_B$ , whilst that

of the Fe-poor site refined to 1.03(3)  $\mu_B$ . Assuming that individual Fe have the same moment at each site, then the refined (average) moments are due to different populations of Fe at each site, which yields  $[\text{Ga}_{0.68(1)}\text{Fe}_{0.32(1)}][\text{Ga}_{0.32(1)}\text{Fe}_{0.68(1)}]\text{O}_3$ , and the equivalent calculation for sample 2 yields  $[\text{Ga}_{0.65(1)}\text{Fe}_{0.35(1)}][\text{Ga}_{0.35(1)}\text{Fe}_{0.65(1)}]\text{O}_3$ . The Rietveld fits are shown together with the refined  $R3c$  model in Figure 5, and refined parameters for each sample are shown in Tables 1 and 2. The consistency between the extent of cation ordering obtained directly from the nuclear scattering, and the extent of ordering obtained independently from the magnetic scattering, in addition to the superior goodness of fit, confirms the assignment of polar  $R3c$  symmetry. The polarization of  $\text{GaFeO}_3$  (sample 1) was calculated as 6.9  $\mu\text{C}\cdot\text{cm}^{-2}$  from a formal point charge model, using the program PSEUDO<sup>46</sup> with the refined atomic coordinates of sample 1.

Anomalous scattering synchrotron X-ray diffraction at the Ga K edge provides an alternative probe of the extent of cation order. The  $R3c$  model was refined simultaneously against two histograms, collected at ambient temperature at resonant (10.359 keV) and non-resonant (15.119 keV) energies from sample 1. The background was fitted by refinement of a Chebyshev polynomial function, and peak profiles were modelled by a Pearson VII function with a refined axial divergence correction. Lattice parameters, atomic coordinates and isotropic thermal displacement parameters were refined independently for each site, and a Suortti surface roughness (absorption) correction was refined for each histogram. Initially a series of  $[\text{Ga}_x\text{Fe}_{1-x}][\text{Ga}_{1-x}\text{Fe}_x]\text{O}_3$  models with the extent of cation ordering ( $x$ ) varied systematically between  $0 \leq x \leq 1$  were refined, and the resulting plot of  $\chi^2$  vs  $x$  (Figure S6) showed two shallow minima centred approximately at  $x = 0.4$  and  $x = 0.6$ , consistent with the partial cation ordering observed by NPD. By allowing  $x$  to refine freely, a composition  $[\text{Ga}_{0.596(4)}\text{Fe}_{0.404(4)}][\text{Ga}_{0.404(4)}\text{Fe}_{0.596(4)}]\text{O}_3$ , which is 19.2(6)% ordered, was obtained which is within four standard deviations of the NPD value (furthermore, the shallow minima in  $\chi^2$  vs  $x$  indicate that the reported least squares errors on  $x$  from SXR D are underestimated). Both the NPD and SXR D results are also consistent with the computational screening of configurational entropy; the average cation order in the 2331 configurations examined and displayed in Figure 3, weighted by their relative population at 900 °C, yields a value of  $[\text{Ga}_{0.61}\text{Fe}_{0.39}][\text{Ga}_{0.39}\text{Fe}_{0.61}]\text{O}_3$ .

HAADF-STEM was used as a local probe to image the cation ordering directly. The two crystallographic positions jointly occupied by Fe and Ga form separate atomic columns in the structure as viewed along the  $[24\bar{6}1]$  ( $= \langle 100 \rangle_p$ ) direction (Figure S7). In HAADF-STEM,

1  
2  
3 the observed intensity is proportional to the composition of the atomic columns and scales  
4 approximately as  $Z^{1.6-1.9}$  (where  $Z$  is the average atomic number of the projected columns).  
5 Because of a very small difference between the average  $Z$  of the Fe-rich and Ga-rich atomic  
6 columns ( $Z = 27.6$  and  $29.4$ , respectively), the associated difference in brightness is expected  
7 to be subtle (see the calculated intensity profile in Figure 6c). Nevertheless, the intensity  
8 profiles taken from the experimental  $[24\bar{6}1]$  HAADF-STEM image (Figure 6a, b) show  
9 systematic intensity differences reminiscent of that observed on the profile from the  
10 calculated image (Figure 6c). All of these structural analyses confirm the  $R3c$  space group  
11 with partial Ga/Fe order in the polar corundum structure.  
12  
13  
14  
15  
16  
17  
18  
19  
20

### 21 3.3. Magnetic order and magnetoelectric coupling

22  
23 Mössbauer spectroscopy of polar corundum  $\text{GaFeO}_3$  at ambient temperature and pressure  
24 confirms the long range magnetic order demonstrated at room temperature by neutron  
25 diffraction (Figure 7d, with fitted parameters shown in Table 3). The absorption pattern is  
26 clearly decomposed into a combination of two magnetically-ordered sites, with average  
27 hyperfine fields of 39.48 T and 33.09 T, respectively (the larger of the two being close to that  
28 of Goethite<sup>47</sup> with its transition temperature of  $\sim 400$  K<sup>48</sup>) which account for 91.09(2) % of the  
29 fitted area, with the remainder assigned to one asymmetric paramagnetic doublet accounting  
30 for 8.91(2) % of the fitted area, which is a dynamic line shape resulting from the proximity of  
31 the Néel temperature. The two main sites exhibit significant static hyperfine field  
32 distributions of width of 0.2 – 0.3 T. The fitted isomer shift (IS) of 0.25 mm/s and quadrupole  
33 splitting of 0.19 mm/s are consistent with  $\text{Fe}^{3+}$ , but the IS is smaller than expected for a  
34 typical octahedral coordination in an oxide, which may be due to the high degree of static  
35 disorder in the system. Isomer shifts of  $<0.25$  mm/s have been reported under applied  
36 hydrostatic pressure for a corundum  $\text{GaFeO}_3$  produced by transformation from the metastable  
37 perovskite (and thus likely to be highly ordered)<sup>25</sup>, demonstrating a high degree of sensitivity  
38 of IS to local coordination environment in this system.  
39  
40  
41  
42  
43  
44  
45  
46  
47  
48  
49  
50

51 Figure 7a shows the magnetisation of polar corundum  $\text{GaFeO}_3$  measured in an applied  
52 magnetic field of 1000 Oe in zero field cooled (ZFC), field cooled (FC) and thermoremanent  
53 magnetisation (TRM) from 300 K to 500 K. ZFC/FC divergence appears at 408 K together  
54 with the onset of TRM. The  $M(H)$  isotherms in Figure 7b are consistent with this magnetic  
55 ordering temperature of 408 K. The linear isotherm at 420K shows that the sample is  
56  
57  
58  
59  
60

1  
2  
3 paramagnetic, with hysteresis observed at and below 400K, consistent with weak  
4 ferromagnetism occurring simultaneously with the antiferromagnetic order. ZFC, FC and  
5 TRM magnetisation data between 5 and 350 K (Figure S8), show that no magnetic transition  
6 occurs below 408K. The remanent magnetisation was  $0.012 \mu_B/\text{f.u.}$  at 10 K (Figure 7b).  
7  
8

9  
10 In order to minimise spurious signals caused by leakage currents, magnetoelectric  
11 measurements were carried out at 10 K on the polar corundum  $\text{GaFeO}_3$  sample poled both  
12 electrically and magnetically (the resistivity at 10 K, measured in-situ, was  $2.38 \times 10^{12} \Omega\cdot\text{m}$ ).  
13 The ME susceptibility ( $\alpha$ ), measured as the slope of the induced ac magnetization ( $M_{ac}$ )  
14 versus the applied ac electric field amplitude ( $E_{ac}$ ) is  $0.057 \text{ ps/m}$ . (Figure 7c). The observation  
15 of linear magnetoelectric coupling is consistent with the symmetry of the magnetic structure:  
16 above the Morin transition,<sup>45</sup>  $\alpha\text{-Fe}_2\text{O}_3$  adopts  $2/m$  magnetic point symmetry (which is  
17 centrosymmetric, permitting weak ferromagnetism but not linear magnetoelectric coupling<sup>49</sup>),  
18 but the cation ordering in polar corundum  $\text{GaFeO}_3$  eliminates the inversion centre, thus  
19 lowering the magnetic point symmetry to  $m$ ,<sup>50</sup> which permits both weak ferromagnetism and  
20 linear magnetoelectric coupling<sup>49</sup>. The observed magnitude of  $\alpha$  is similar to that observed in  
21 other Fe-based polar magnetoelectrics that are ordered magnetically above room  
22 temperature.<sup>10, 12, 51</sup> Demonstration of switchable electrical polarization (*i.e.* ferroelectricity  
23 and multiferroicity) was not possible in these samples due to the high dielectric loss.  
24  
25  
26  
27  
28  
29  
30  
31  
32  
33  
34  
35  
36  
37  
38

### 39 3.4. Thermal stability

40  
41 To test the thermal stability and decomposition behaviour of polar corundum  $\text{GaFeO}_3$  at  
42 ambient pressure, the as-made samples were annealed at different temperatures between 300  
43 – 1000 °C in air. Ex-situ PXRD patterns of the post-annealed samples showed that the  
44 orthorhombic ambient pressure phase is recovered after annealing at 1000 °C, but the  
45 corundum unit cell is retained after annealing at 300 – 800 °C with no apparent  
46 decomposition (Figure S9). However, DSC and in-situ dielectric measurements (Figure 8)  
47 collected on heating from 25 – 500 °C show an endothermic peak, and a corresponding peak  
48 in the dielectric constant, which is frequency-independent (Figure S10) and centred at  
49 approximately 200 °C. The feature is strongly pronounced during the first heating cycle and  
50 absent in subsequent cycles, which indicates the occurrence of an irreversible phase  
51 transition. To investigate whether this is associated with a loss of polarity in the sample,  
52  
53  
54  
55  
56  
57  
58  
59  
60

1  
2  
3 CBED images, magnetisation and magnetoelectric coupling data were collected on annealed  
4 samples.  
5

6 Figure 7c shows the ME susceptibility  $\alpha$  decreases from 0.057 ps/m for as-made polar  
7 corundum GaFeO<sub>3</sub> to 0.003 ps/m for the sample annealed at 380 °C: for this sample, the  
8 induced magnetic moment is below the detection limit of 10<sup>-9</sup> emu. Close inspection of the  
9 CBED whole pattern symmetry for the  $[\bar{1}11]$  zone axis (Figure S11) reveals the sample to  
10 have retained 3*m* point symmetry, which implies that the sample has retained some residual  
11 polarity. Taken together with the magnetoelectric measurements, this implies that the polarity  
12 of the material (via the cation ordering) is diminished, but not eliminated entirely, by  
13 annealing polar corundum GaFeO<sub>3</sub> at this temperature. The weak ferromagnetism, which  
14 arises from the  $\alpha$ -Fe<sub>2</sub>O<sub>3</sub>-type magnetic structure, is also retained after thermal treatment  
15 (Figure S12). This is consistent with the 2/*m* magnetic point symmetry of  $\alpha$ -Fe<sub>2</sub>O<sub>3</sub> above the  
16 Morin transition<sup>45</sup>: the loss of cation ordering in polar corundum GaFeO<sub>3</sub> would restore the  
17 inversion centre, thus raising the magnetic point symmetry back to 2/*m* (which is  
18 centrosymmetric, permitting weak ferromagnetism but not linear magnetoelectric coupling<sup>49</sup>).  
19  
20  
21  
22  
23  
24  
25  
26  
27  
28

#### 29 4. Discussion

30 Under the high temperature, high pressure conditions applied in this study, a corundum phase  
31 of GaFeO<sub>3</sub> forms directly from the ambient pressure phase, in contrast to the sequence of  
32 phases observed on application of pressure at room temperature where a corundum phase is  
33 accessed via a non-quenchable perovskite phase<sup>25</sup>. The fact that the phase does not form by  
34 transformation from the high pressure perovskite phase<sup>18, 25</sup> means that the extent of Ga/Fe  
35 ordering is limited, producing the polar corundum structure rather than the fully ordered  
36 LiNbO<sub>3</sub> structure. NPD and X-ray anomalous scattering experiments demonstrate a greater  
37 degree of ordering in GaFeO<sub>3</sub> than in the isostructural ScFeO<sub>3</sub>. Our computational results  
38 imply that GaFeO<sub>3</sub> should have a greater tendency towards cation disorder than ScFeO<sub>3</sub> at a  
39 given synthesis temperature, as demonstrated by the higher number of accessible cation  
40 configurations in GaFeO<sub>3</sub> (Figure 3). This originates from the small overall energy cost of  
41 Ga/Fe site swaps in GaFeO<sub>3</sub>, while only the antisite Sc/Fe defect within face-shared dimers is  
42 energetically possible in ScFeO<sub>3</sub>. While the enthalpy of the polar corundum phase of both  
43 GaFeO<sub>3</sub> and ScFeO<sub>3</sub> is unstable relative to the binary oxides, the higher entropic content of  
44 GaFeO<sub>3</sub> (provided by the large number of thermally accessible cation configurations in the  
45 corundum cell at the synthesis temperature) means that its polar corundum phase is stabilised  
46 at lower temperature than that of ScFeO<sub>3</sub>. Experimentally, this results in polar corundum  
47  
48  
49  
50  
51  
52  
53  
54  
55  
56  
57  
58  
59  
60

1  
2  
3 GaFeO<sub>3</sub> being stabilized at 900 °C, while polar corundum ScFeO<sub>3</sub> must be synthesized at a  
4 much higher temperature of 1400 °C. The effect of the different synthesis temperatures of the  
5 two materials is expected to have an impact on the extent of cation ordering. From our  
6 previous Monte Carlo simulation of ScFeO<sub>3</sub><sup>14</sup>, it was clear that between 1300 and 1450 K,  
7 ScFeO<sub>3</sub> transformed from a mainly ordered to a mainly disordered structure: it is also clear  
8 that ScFeO<sub>3</sub> is calculated to be much more ordered than GaFeO<sub>3</sub> at 1200 K, with a site  
9 occupancy of ~0.9. This indicates that the experimentally observed cation disorder in polar  
10 corundum ScFeO<sub>3</sub> is driven by the enhanced configurational entropy at the higher synthesis  
11 temperature. In GaFeO<sub>3</sub>, the low synthesis temperature of 900 °C provides sufficient  
12 configurational entropy to stabilise the polar corundum, but it is insufficient to disorder the  
13 material to the same extent as seen for ScFeO<sub>3</sub> synthesised at 1400 °C, and consequently  
14 produces more ordered compounds. We note the creation of anti-site defects in LiNbO<sub>3</sub>-type  
15 GaFeO<sub>3</sub> (*e.g.* by swapping cations in adjacent face-sharing MO<sub>6</sub> octahedra, as described in  
16 Supporting Information) is less energetically demanding than in LiNbO<sub>3</sub>-type ScFeO<sub>3</sub>, see  
17 Table S2, and the anti-site defects may be partly responsible for the cation disorder in polar  
18 corundum GaFeO<sub>3</sub>. It is possible that another source of disorder could originate from the  
19 precursor of corundum GaFeO<sub>3</sub>, *i.e.* the ambient pressure AlFeO<sub>3</sub>-type, in which extent of  
20 cation ordering is dependent on the synthesis conditions<sup>52</sup> and predicted from our simulation  
21 based on small energy costs of creating anti-site defects (see Table S6 in the Supporting  
22 Information). This implies that a more ordered polar corundum GaFeO<sub>3</sub> may be obtained  
23 from a highly ordered precursor, *e.g.* the fully ordered perovskite, as observed experimentally  
24 in ScFeO<sub>3</sub><sup>18</sup>.

25  
26  
27  
28  
29  
30  
31  
32  
33  
34  
35  
36  
37  
38  
39  
40 In most respects the refined crystal structure of GaFeO<sub>3</sub> is very similar to that of ScFeO<sub>3</sub>. The  
41 unit cell volume of GaFeO<sub>3</sub> is approximately 10 % smaller than that of ScFeO<sub>3</sub> on account of  
42 the smaller ionic radius of Ga<sup>3+</sup> (0.62 Å) versus Sc<sup>3+</sup> (0.745 Å). This is an isotropic  
43 contraction driven by the smaller average size of the MO<sub>6</sub> coordination octahedra, as  
44 indicated by the similar *c/a* ratios in the two compounds (2.71 and 2.69, respectively). The  
45 unit cell dimensions of GaFeO<sub>3</sub> are very close to those of α-Fe<sub>2</sub>O<sub>3</sub><sup>41-42</sup> and are consistent with  
46 those reported from corundum structured GaFeO<sub>3</sub> in a recent in-situ high pressure study<sup>25</sup>.  
47 The refined metal-oxide distances, illustrated in Figure 5, lie in the range 1.93 – 2.13 Å, and  
48 the refined volume of the Ga-rich MO<sub>6</sub> polyhedra (10.49 Å<sup>3</sup>) are slightly smaller than those of  
49 the Fe-rich polyhedra (10.64 Å<sup>3</sup>), consistent with the relative ionic radii. As in the binary  
50  
51  
52  
53  
54  
55  
56  
57  
58  
59  
60



1  
2  
3 corundums and  $\text{ScFeO}_3$ , the cations are displaced from the centres of the face-sharing  $\text{MO}_6$   
4 octahedra by electrostatic repulsion.  
5  
6

7 Polar corundum  $\text{GaFeO}_3$  exhibits weak ferromagnetism with an ordering temperature of 408  
8 K; this is approximately 50 K higher than the ordering temperature observed in  $\text{ScFeO}_3$ <sup>14</sup>,  
9 which may be due to its enhanced cation ordering. The remanent magnetisation of  $\text{GaFeO}_3$   
10 (0.012  $\mu_{\text{B}}$  / f.u.) is comparable to that observed in  $\text{ScFeO}_3$  (0.0106  $\mu_{\text{B}}$  / f.u.)<sup>14</sup>. The  
11 combination of weak ferromagnetism and absence of inversion symmetry permits  
12 magnetoelectric coupling in  $\text{GaFeO}_3$ . The observed linear magnetoelectric susceptibility ( $\alpha$ )  
13 of 0.057 ps m<sup>-1</sup> is small in comparison to other Fe-based polar weak ferromagnetic  
14 ceramics<sup>10, 51</sup>, but the fact that the room temperature structure is identical to the structure at  
15 the measurement temperature (10 K) implies that, given definition of a suitable processing  
16 protocol, magnetoelectric coupling may be attainable under ambient conditions in this  
17 compound. The magnitude of this coupling falls below a detectable value when the sample is  
18 heated to 380 °C at ambient pressure. DSC and dielectric measurements suggest that this is  
19 due to an irreversible phase transition, CBED patterns however indicate that  $3m$  point  
20 symmetry is still present in the sample. This indicates that the polarity of the sample (driven  
21 by the cation ordering that defines the polar corundum structure type) is degraded sufficiently  
22 to weaken the ME response below the detection limit, but is not entirely eliminated by  
23 annealing under these conditions. Ultimately, the ambient pressure phase is recovered by  
24 annealing at a sufficiently high temperature.  
25  
26  
27  
28  
29  
30  
31  
32  
33  
34  
35  
36  
37

## 38 5. Conclusions

39  
40  $\text{GaFeO}_3$  is the second member of the polar corundum family, and the first to display ME  
41 coupling. The enhanced cation site order in  $\text{GaFeO}_3$  over  $\text{ScFeO}_3$  confirms the distinction of  
42 this family both from non-polar corundum and from fully  $\text{LiNbO}_3$ -ordered derivatives: the  
43 less extreme synthesis conditions required to access polar corundum indicate that a broad  
44 family of materials should be accessible, for example through multiple cation decoration of  
45 corundum.  
46  
47  
48  
49

50  
51 The magnetoelectric coupling shows that the engineered co-existence of magnetisation and  
52 polarisation in new structural families is a route to coupling these degrees of freedom – thin  
53 film growth, already achieved for  $\text{ScFeO}_3$ <sup>14</sup>, is a route to tune this further. The relationship  
54 between  $M$ ,  $\alpha$  and the cation site order is also controllable via site-ordering extent. The  
55 absence of measurable magnetic impurities under the optimised synthesis conditions is  
56  
57  
58  
59  
60

1  
2  
3 consistent with the stability and chemical robustness of this new family of room temperature  
4 polar magnetic magnetoelectric materials.  
5  
6  
7  
8  
9  
10  
11  
12  
13  
14  
15  
16  
17  
18  
19  
20  
21  
22  
23  
24  
25  
26  
27  
28  
29  
30  
31  
32  
33  
34  
35  
36  
37  
38  
39  
40  
41  
42  
43  
44  
45  
46  
47  
48  
49  
50  
51  
52  
53  
54  
55  
56  
57  
58  
59  
60

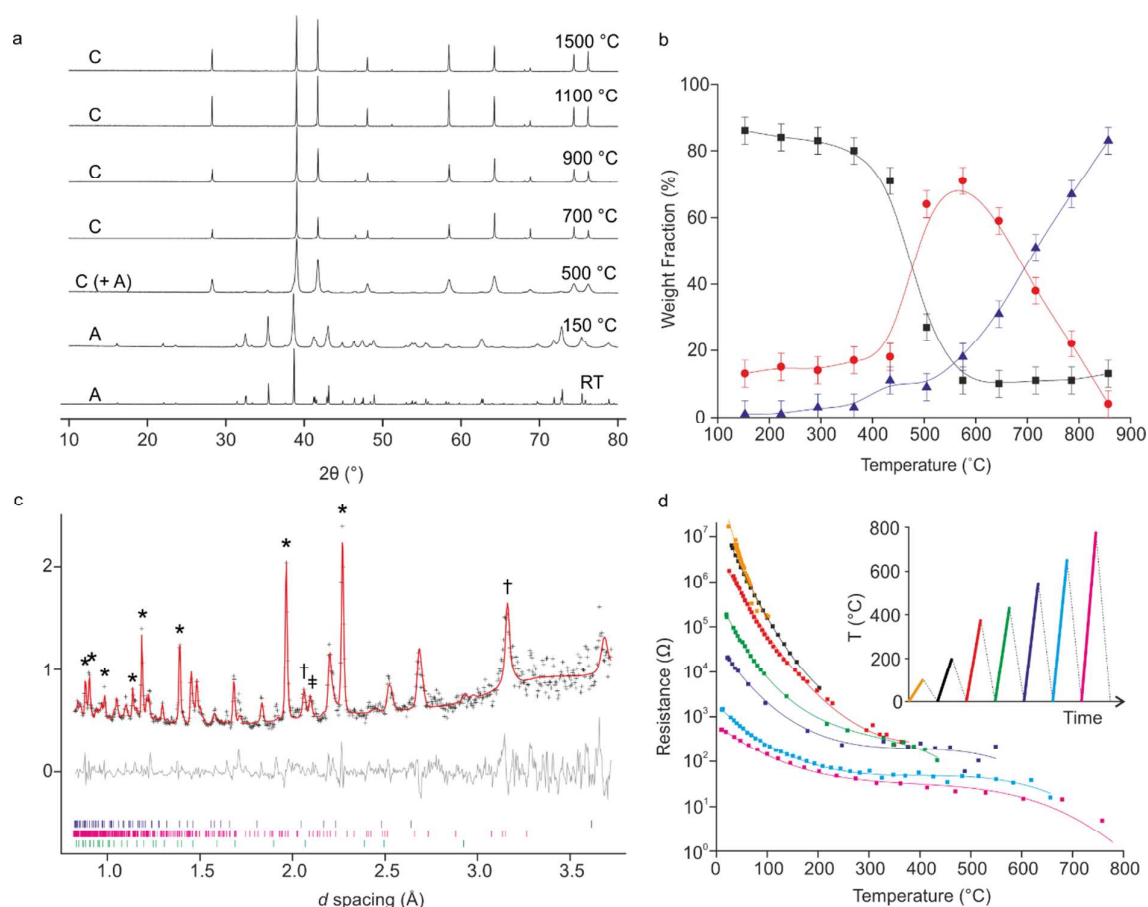


**Figure 1:** Formation of the corundum phase by high temperature high pressure annealing. (a) Laboratory PXRD patterns obtained from GaFeO<sub>3</sub> quenched from a range of temperatures after annealing at 6 GPa. Patterns labelled A contain the starting AlFeO<sub>3</sub>-structured phase, and those labelled C contain the corundum phase. (b) Refined weight fraction of the AlFeO<sub>3</sub> (black), corundum (red) phases and spinel decomposition phase (blue) as a function of temperature at 6 GPa from in-situ neutron diffraction. (c) Rietveld refinement against in-situ neutron data collected at 6 GPa, 500 °C. Blue tick marks = corundum phase, magenta = AlFeO<sub>3</sub> phase, green = spinel phase. Asterisks (\*) mark peaks from the Pt pressure calibrant; daggers (†) mark graphite peaks, double dagger (‡) marks a vanadium peak. (d) In-situ resistance measurements collected from a pellet of GaFeO<sub>3</sub> at 6 GPa cycled to increasing temperatures. Lines are a guide to the eye. The colours of the points correspond to their position in the heating sequence, which is shown inset.

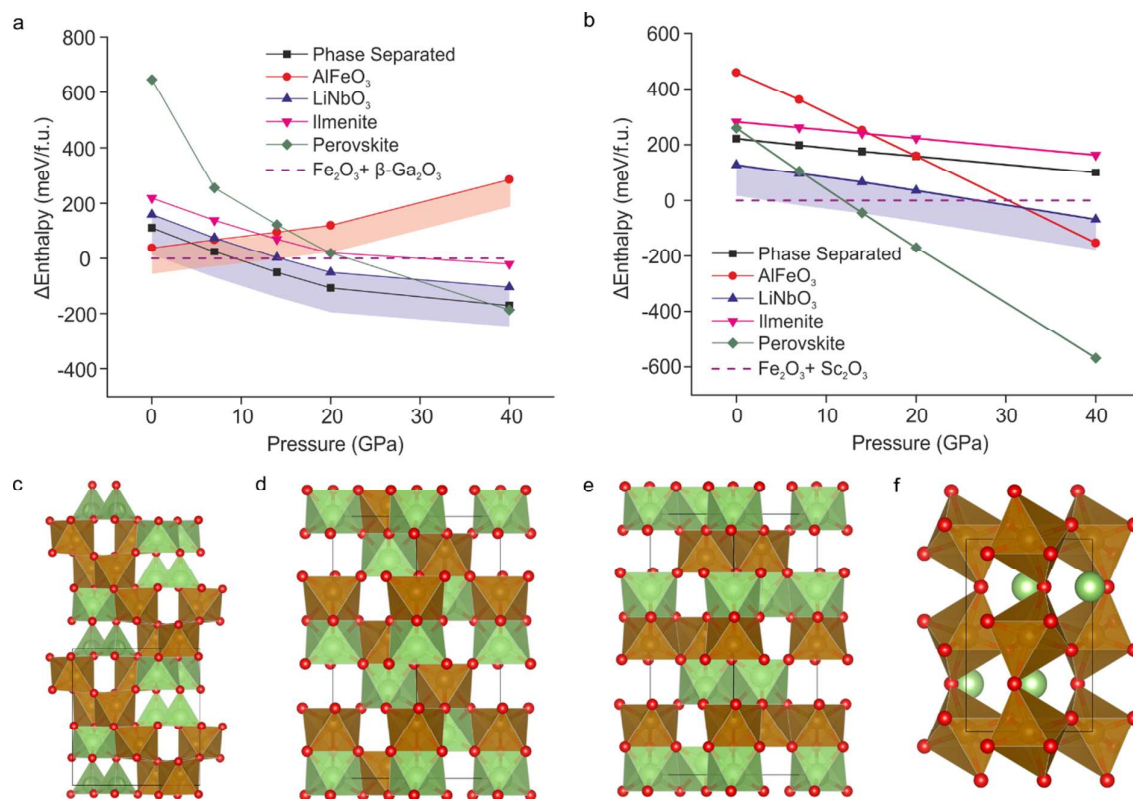


**Figure 2:** Calculated enthalpies as a function of pressure for (a) GaFeO<sub>3</sub> polymorphs in the AFM state, and (b) ScFeO<sub>3</sub> polymorphs in the AFM state, plotted relative to the binary oxides  $\alpha$ -Fe<sub>2</sub>O<sub>3</sub> +  $\beta$ -Ga<sub>2</sub>O<sub>3</sub> and  $\alpha$ -Fe<sub>2</sub>O<sub>3</sub> + Sc<sub>2</sub>O<sub>3</sub>. The shaded areas represent an estimate of the configurational entropy of GaFeO<sub>3</sub> and ScFeO<sub>3</sub> at the respective synthesis temperatures of 1200 K and 1800 K: 98.8 meV/f.u. for the ambient pressure AlFeO<sub>3</sub>-type GaFeO<sub>3</sub>; 143 meV/f.u. for corundum GaFeO<sub>3</sub> and 106 meV/f.u. for corundum ScFeO<sub>3</sub>. (c) the ambient pressure AlFeO<sub>3</sub>-type structure of GaFeO<sub>3</sub> viewed along [001], which features edge-sharing chains of (Fe, Ga) octahedra parallel to vertex-linked GaO<sub>4</sub> tetrahedra, (d) the polar LiNbO<sub>3</sub>-type cation ordering in the corundum structure, (e) the non-polar FeTiO<sub>3</sub> (ilmenite)-type cation ordering in the corundum structure, (f) the optimised *Pbnm* perovskite-type structure used for this calculation, which represents the phase that is accessible experimentally under applied pressures of 25 GPa<sup>25</sup>. Atom colours: green = Ga(Sc), brown = Fe, red = O.

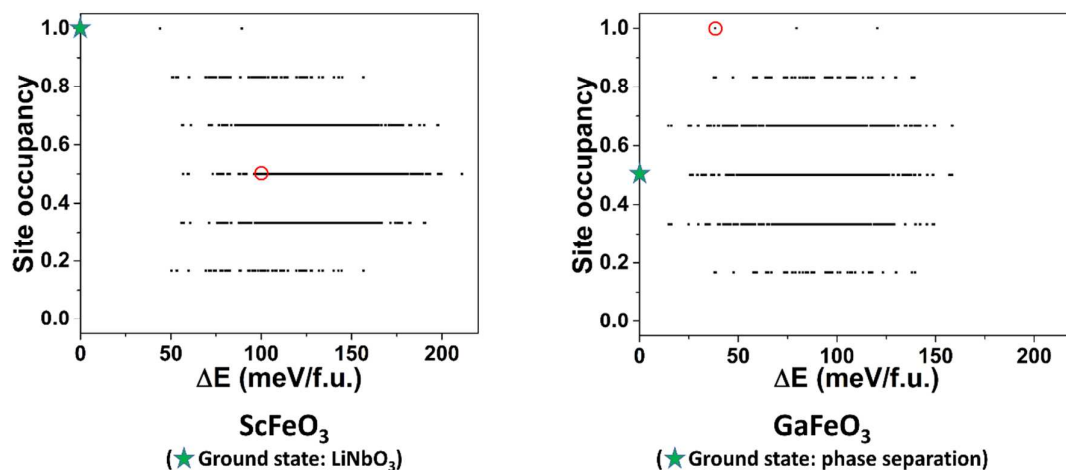


**Figure 3:** Calculated stabilities of different cation configurations in a hexagonal corundum-type unit cell. Site occupancies (defined as the proportion of  $\text{Fe}^{3+}$  cations in a given configuration that are coincident with  $\text{Fe}^{3+}$  positions in the fully ordered  $\text{LiNbO}_3$  structure) of different configurations are plotted against their relative energies with respect to the ground state of  $\text{ScFeO}_3$  (left) and  $\text{GaFeO}_3$  (right). The phase separated structure of  $\text{ScFeO}_3$  and the  $\text{LiNbO}_3$ -type  $\text{GaFeO}_3$  are highlighted in red circles. The lowest energy configuration is marked with a green star symbol.

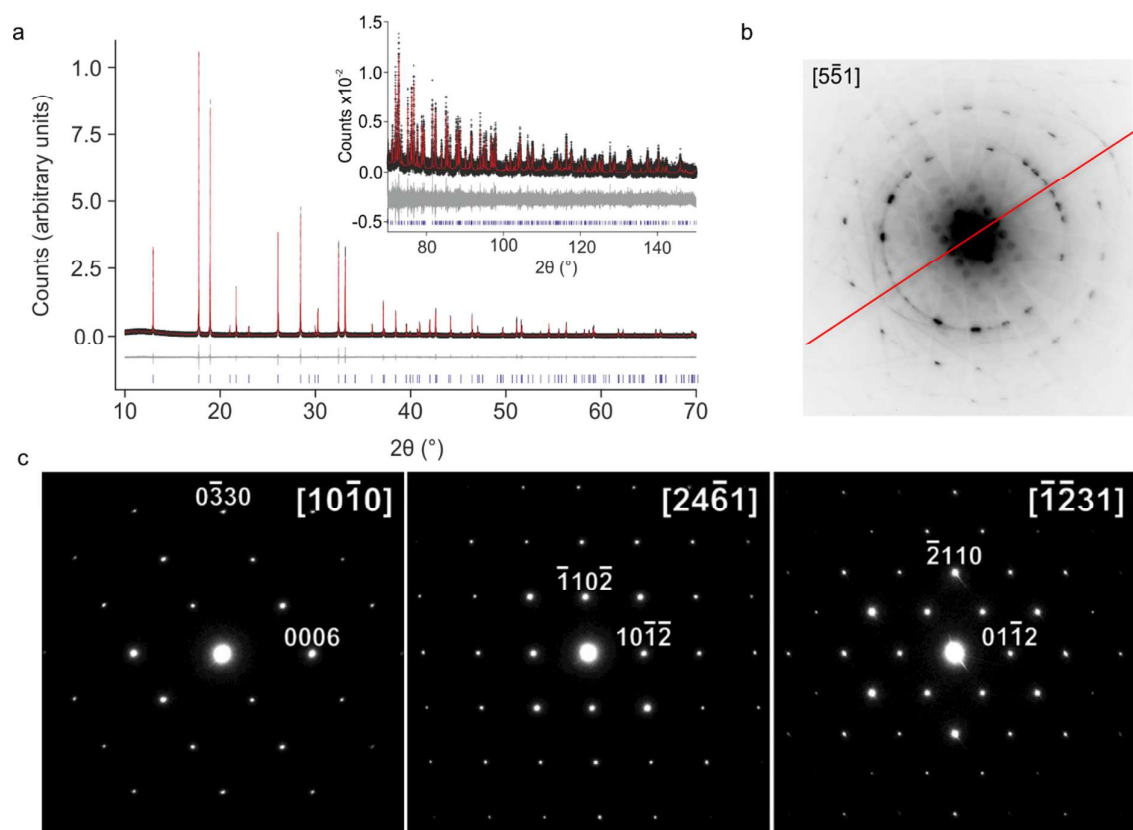


**Figure 4:** Unit cell and space group determination. (a) LeBail fit to SXRD data ( $\lambda = 0.8256185 \text{ \AA}$ ) of corundum  $\text{GaFeO}_3$  in the hexagonal setting of space group  $R\bar{3}c$ , which has the highest symmetry consistent with the systematic absences, yields a refined unit cell of dimensions  $a = 5.01959(3)$ ,  $c = 13.5907(2) \text{ \AA}$ . The fit to high angle data ( $70 < 2\theta < 150^\circ$ ) is inset. Black markers =  $y_{\text{obs}}$ , red line =  $y_{\text{calc}}$ , grey line =  $y_{\text{obs}} - y_{\text{calc}}$ , blue tick marks = allowed  $hkl$  reflections. (b) CBED  $[5\bar{5}1]$  zone axis pattern of corundum  $\text{GaFeO}_3$ , which contains a mirror plane as the only symmetry element, consistent with space group  $R3c$ . (c) SAED patterns from three different zone axes, confirming the rhombohedral cell and systematic absences observed by SXRD.

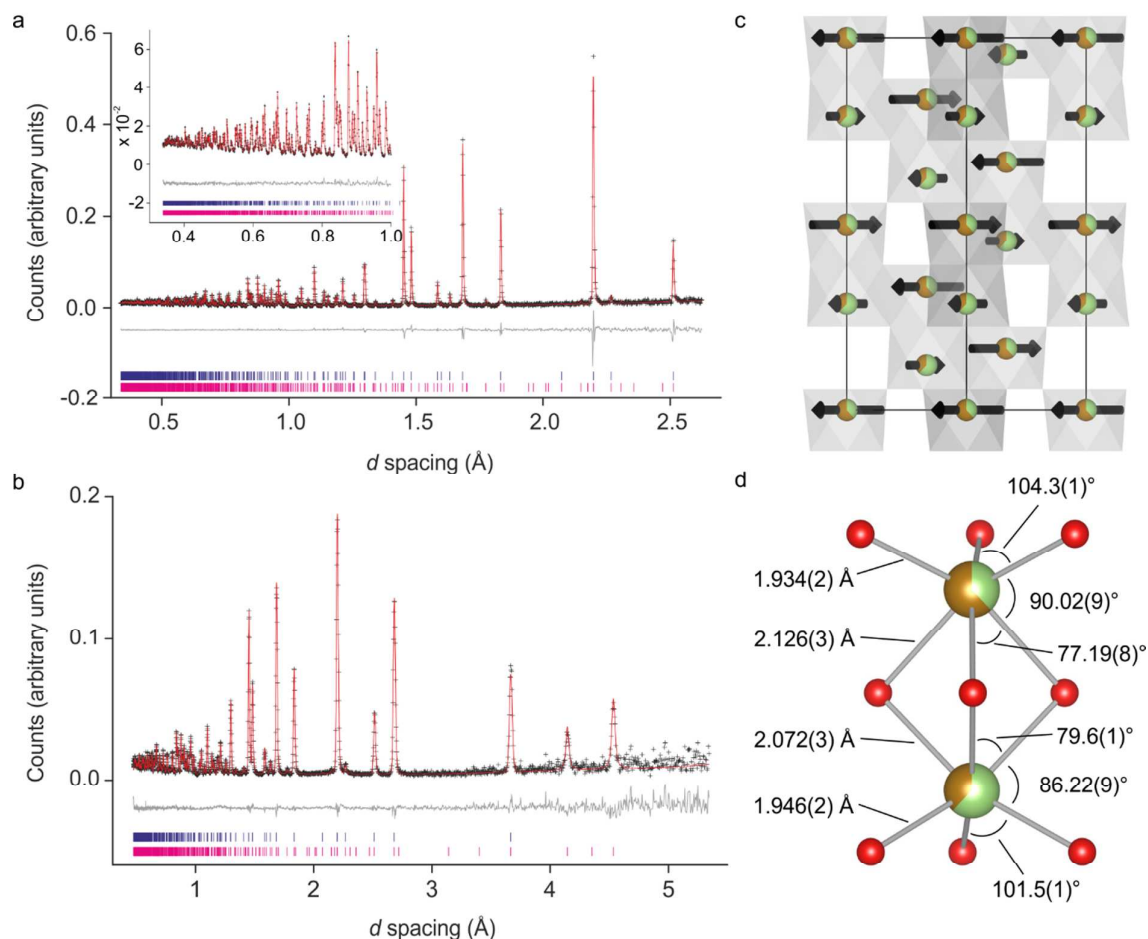


**Figure 5:** Refined polar corundum structure of GaFeO<sub>3</sub>. (a) Rietveld refinement against NPD data from the Polaris back-scattering bank (inset: fit to the low  $d$ -spacing region), and (b) against Polaris bank 3 ( $2\theta = 52.2^\circ$ ), which features two intense peaks of magnetic origin in the range  $4 < d < 5$  Å; black markers =  $y_{\text{obs}}$ , red line =  $y_{\text{calc}}$ , grey line =  $y_{\text{obs}} - y_{\text{calc}}$ , blue tick marks = nuclear structure, magenta tick marks = magnetic structure. (c) The refined nuclear and magnetic structure of GaFeO<sub>3</sub> viewed along  $110$ . At each atom, green segments indicate Ga occupancy, brown segments indicate Fe occupancy, black arrows indicate magnetic moments which are ordered parallel to the  $a$  axis in an antiferromagnetic arrangement. The magnitudes of the ordered moments are indicated by the sizes of the arrows. (d) The local coordination environments of the two crystallographically independent cation sites, which occupy adjacent face-sharing octahedra. The colours indicate the extent of occupancy by Fe (brown) and Ga (green).



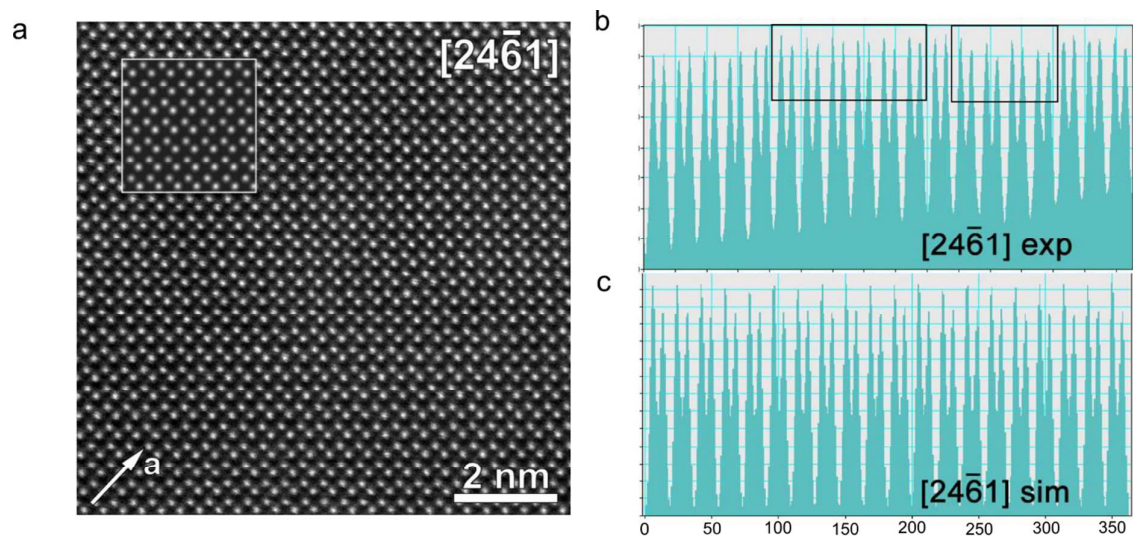


**Figure 6:** HAADF-STEM analysis of polar corundum  $\text{GaFeO}_3$  (a) Experimental HAADF-STEM image from the  $[24\bar{6}1]$  axis, with a simulated image (inset) generated from the refined (PND) crystal structure. (b) Intensity profiles measured from individual rows of atomic columns over large areas from the experimental image, and (c) intensity profiles measured over large areas from the simulated image. Regions in (b) that resemble the simulated structure of (c) are marked with black rectangles.



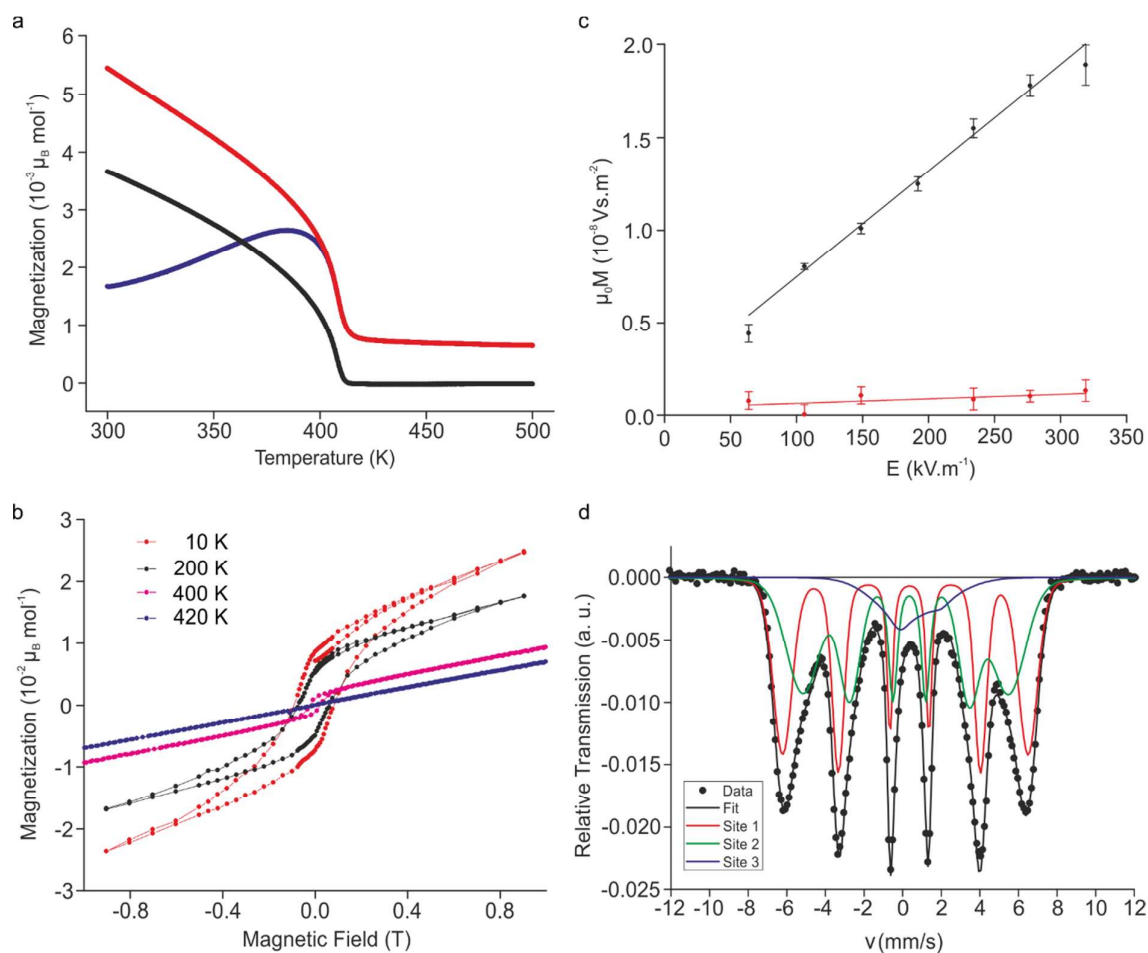


**Figure 7.** Magnetic properties of polar corundum GaFeO<sub>3</sub>. (a) Zero-field cooled (blue points), field-cooled (red points) and remanent (black) magnetization as a function of temperature in the range 300 – 500 K, measured with an applied field of 0.1 T. (b) Magnetization as a function of applied magnetic field at temperatures of 10 K (red points), 200 K (black points), 400 K (magenta points) and 420 K (blue points). (c) Induced ac magnetization versus applied ac electric field amplitude at 10 K for two samples: as-made (black points), and post-annealed at 380 °C (red points). (d)  $^{57}\text{Fe}$  Mössbauer spectrum at ambient temperature, showing hyperfine splitting consistent with long-range magnetic ordering, and fitted with a three-site model (see Table 3 for fitted parameters).

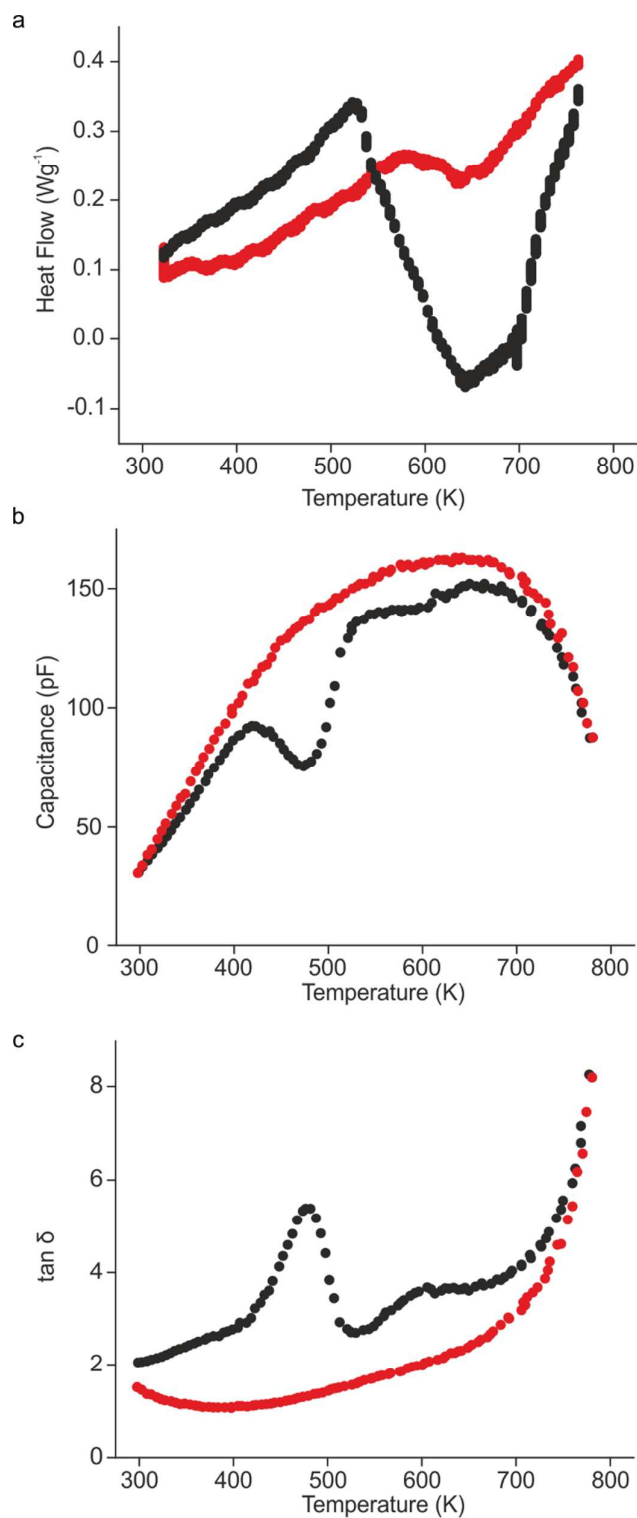


**Figure 8:** Calorimetric and dielectric behaviour of polar corundum GaFeO<sub>3</sub> synthesised at 900 °C. (a) DSC scans performed on heating, black points represent the first cycle and red points represent the second cycle. (b) Capacitance data recorded on first heating cycle (black points) and second heating cycle (red points). (c) Dielectric loss recorded on first heating cycle (black points) and second heating cycle (red points).

**Table 1:** Structural parameters for  $R3c$  GaFeO<sub>3</sub> (sample 1) from Rietveld refinement against room temperature NPD, with refined lattice parameters  $a = 5.01871(9)$  Å,  $c = 13.5879(3)$  Å,  $V = 296.39(1)$  Å<sup>3</sup>.

	x	y	z	B <sub>iso</sub> / Å <sup>2</sup>	Occ.	M / μ <sub>B</sub>
Ga(1)	0	0	0	0.231(3)	0.32(2)	
Fe(1)	0	0	0	0.231(3)	0.68(2)	1.03(3)
Fe(2)	0	0	0.28919(5)	0.231(3)	0.32(2)	2.15(2)
Ga(2)	0	0	0.28919(5)	0.231(3)	0.68(2)	
O(1)	0.3026(2)	-0.0046(4)	0.8922(3)	0.284 (5)	1	

**Table 2:** Structural parameters for  $R3c$  GaFeO<sub>3</sub> (sample 2) refined against room temperature NPD data, with refined lattice parameters  $a = 5.02547(9)$  Å,  $c = 13.6057(3)$  Å,  $V = 297.31$  (2) Å<sup>3</sup>.

	x	y	z	B <sub>iso</sub> / Å <sup>2</sup>	Occ.	M / μ <sub>B</sub>
Ga(1)	0	0	0	0.216(4)	0.38(3)	
Fe(1)	0	0	0	0.216(4)	0.62(3)	1.08(4)
Fe(2)	0	0	0.28906(5)	0.216(4)	0.38(3)	2.00(3)
Ga(2)	0	0	0.28906(5)	0.216(4)	0.62(3)	
O(1)	0.3030(3)	-0.0033(5)	0.8916(2)	0.34(2)	1	

**Table 3:** Mössbauer fitting parameters for the spectrum of Figure 7. The errors are provided in brackets.

Site	B <sub>hf</sub> (T)	ΔB <sub>hf</sub> (T)	IS (mm/s)	QS (mm/s)	A (%)
1	39.49(2)	0.28(1)	0.249(3)	0.21(1)	44.00(1)
2	33.11(2)	0.37(1)	0.257(3)	0.19(1)	47.09(1)
3	0	0	0.93(1)	2.16(3)	8.91(1)

**Acknowledgements**

This work was funded by the EPSRC under EP/N004884. We thank the STFC for provision of beam time at ISIS and Diamond Light Source. We thank the Materials Chemistry Consortium (EPSRC, EP/L000202) for access to computer time on the ARCHER UK National Supercomputing Service (<http://www.archer.ac.uk>). AMA is grateful to the Russian Science Foundation (grant 14-13-00680) for financial support. MJR is a Royal Society Research Professor. We wish to thank Dr. Ming Li (University of Nottingham, UK) for helpful discussion and advice.

## References

1. Scott, J. F., *Nat. Mater.* **2007**, *6* (4), 256-257.
2. Bibes, M.; Barthelemy, A., *Nat. Mater.* **2008**, *7* (6), 425-426.
3. Hill, N. A., *J. Phys. Chem. B* **2000**, *104* (29), 6694-6709.
4. Hill, N. A.; Filippetti, A., *J. Magn. Magn. Mater.* **2002**, *242*, 976-979.
5. Khomskii, D. I., *J. Magn. Magn. Mater.* **2006**, *306* (1), 1-8.
6. Sando, D.; Barthélémy, A.; Bibes, M., *J. Phys.: Condens. Matter* **2014**, *26* (47), 473201.
7. Catalan, G.; Scott, J. F., *Adv. Mater.* **2009**, *21* (24), 2463-2485.
8. Wang, J.; Neaton, J. B.; Zheng, H.; Nagarajan, V.; Ogale, S. B.; Liu, B.; Viehland, D.; Vaithyanathan, V.; Schlom, D. G.; Waghmare, U. V.; Spaldin, N. A.; Rabe, K. M.; Wuttig, M.; Ramesh, R., *Science* **2003**, *299* (5613), 1719-1722.
9. Heron, J. T.; Trassin, M.; Ashraf, K.; Gajek, M.; He, Q.; Yang, S. Y.; Nikonov, D. E.; Chu, Y. H.; Salahuddin, S.; Ramesh, R., *Phys. Rev. Lett.* **2011**, *107* (21).
10. Mandal, P.; Pitcher, M. J.; Alaria, J.; Niu, H.; Borisov, P.; Stamenov, P.; Claridge, J. B.; Rosseinsky, M. J., *Nature* **2015**, *525* (7569), 363-366.
11. Benedek, N. A.; Fennie, C. J., *Phys. Rev. Lett.* **2011**, *106* (10).
12. Pitcher, M. J.; Mandal, P.; Dyer, M. S.; Alaria, J.; Borisov, P.; Niu, H.; Claridge, J. B.; Rosseinsky, M. J., *Science* **2015**, *347* (6220), 420-424.
13. Alaria, J.; Borisov, P.; Dyer, M. S.; Manning, T. D.; Lepadatu, S.; Cain, M. G.; Mishina, E. D.; Sherstyuk, N. E.; Ilyin, N. A.; Hadermann, J.; Lederman, D.; Claridge, J. B.; Rosseinsky, M. J., *Chem. Sci.* **2014**, *5* (4), 1599-1610.
14. Li, M.-R.; Adem, U.; McMitchell, S. R. C.; Xu, Z.; Thomas, C. I.; Warren, J. E.; Giap, D. V.; Niu, H.; Wan, X.; Palgrave, R. G.; Schiffmann, F.; Cora, F.; Slater, B.; Burnett, T. L.; Cain, M. G.; Abakumov, A. M.; van Tendeloo, G.; Thomas, M. F.; Rosseinsky, M. J.; Claridge, J. B., *J. Am. Chem. Soc.* **2012**, *134* (8), 3737-3747.

- 1  
2  
3 15. Li, M. R.; Walker, D.; Retuerto, M.; Sarkar, T.; Hadermann, J.; Stephens, P. W.; Croft, M.;  
4 Ignatov, A.; Grams, C. P.; Hemberger, J.; Nowik, I.; Halasyamani, P. S.; Tran, T. T.; Mukherjee,  
5 S.; Dasgupta, T. S.; Greenblatt, M., *Angew. Chem. Int. Ed.* **2013**, *52* (32), 8406-8410.  
6  
7  
8 16. Li, M. R.; Stephens, P. W.; Retuerto, M.; Sarkar, T.; Grams, C. P.; Hemberger, J.; Croft, M. C.;  
9 Walker, D.; Greenblatt, M., *J. Am. Chem. Soc.* **2014**, *136* (24), 8508-8511.  
10  
11  
12 17. Ye, M.; Vanderbilt, D., *Phys. Rev. B* **2016**, *93* (13), 134303.  
13  
14  
15 18. Kawamoto, T.; Fujita, K.; Yamada, I.; Matoba, T.; Kim, S. J.; Gao, P.; Pan, X.; Findlay, S. D.;  
16 Tassel, C.; Kageyama, H.; Studer, A. J.; Hester, J.; Irifune, T.; Akamatsu, H.; Tanaka, K., *J. Am.*  
17 *Chem. Soc.* **2014**, *136* (43), 15291-15299.  
18  
19  
20 19. Bréard, Y.; Fjellvåg, H.; Hauback, B., *Solid State Commun.* **2011**, *151* (3), 223-226.  
21  
22  
23 20. Sharma, K.; Reddy, V. R.; Gupta, A.; Kaushik, S. D.; Siruguri, V., *J. Phys.: Condens. Matter*  
24 **2012**, *24* (37).  
25  
26  
27 21. Uk Kang, K.; Baek Kim, S.; Yong An, S.; Cheong, S.-W.; Sung Kim, C., *J. Magn. Magn. Mater.*  
28 **2006**, *304* (2), e769-e771.  
29  
30  
31 22. O'Dell, T. H., *Int. J. Magn.* **1973**, *4* (3), 239-244.  
32  
33  
34 23. Arima, T.; Higashiyama, D.; Kaneko, Y.; He, J. P.; Goto, T.; Miyasaka, S.; Kimura, T.; Oikawa,  
35 K.; Kamiyama, T.; Kumai, R.; Tokura, Y., *Phys. Rev. B* **2004**, *70* (6), 064426.  
36  
37  
38 24. Fujita, K.; Kawamoto, T.; Yamada, I.; Hernandez, O.; Hayashi, N.; Akamatsu, H.; Lafargue-Dit-  
39 Hauret, W.; Rocquefelte, X.; Fukuzumi, M.; Manuel, P.; Studer, A. J.; Knee, C. S.; Tanaka, K.,  
40 *Chem. Mater.* **2016**, *28* (18), 6644-6655.  
41  
42  
43 25. Arielly, R.; Xu, W. M.; Greenberg, E.; Rozenberg, G. K.; Pasternak, M. P.; Garbarino, G.; Clark,  
44 S.; Jeanloz, R., *Phys. Rev. B* **2011**, *84* (9), 094109.  
45  
46  
47 26. Marezio, M.; Remeika, J. P., *J. Chem. Phys.* **1967**, *46* (5), 1862-1865.  
48  
49  
50 27. Bull, C. L.; Funnell, N. P.; Tucker, M. G.; Hull, S.; Francis, D. J.; Marshall, W. G., *High Pressure*  
51 *Res.* **2016**, 1-19.  
52  
53  
54 28. Klotz, S.; Le Godec, Y.; Straessle, T.; Stuhr, U., *Appl. Phys. Lett.* **2008**, *93* (9).  
55  
56  
57  
58  
59  
60

- 1  
2  
3 29. Zha, C.-S.; Mibe, K.; Bassett, W. A.; Tschauer, O.; Mao, H.-K.; Hemley, R. J., *J. Appl. Phys.* **2008**, *103* (5), 054908.  
4  
5  
6  
7 30. Le Godec, Y.; Dove, M. T.; Francis, D. J.; Kohn, S. C.; Marshall, W. G.; Pawley, A. R.; Price, G.  
8 D.; Redfern, S. A. T.; Rhodes, N.; Ross, N. L.; Schofield, P. F.; Schooneveld, E.; Syfosse, G.;  
9 Tucker, M. G.; Welch, M. D., *Mineral. Mag.* **2001**, *65* (6), 737-748.  
10  
11  
12 31. Borisov, P.; Hochstrat, A.; Shvartsman, V. V.; Kleemann, W., *Rev. Sci. Instrum.* **2007**, *78* (10),  
13 106105.  
14  
15  
16 32. VandeVondele, J.; Krack, M.; Mohamed, F.; Parrinello, M.; Chassaing, T.; Hutter, J., *Comput.*  
17 *Phys. Commun.* **2005**, *167* (2), 103-128.  
18  
19  
20 33. Hutter, J.; Iannuzzi, M.; Schiffmann, F.; VandeVondele, J., *Wiley Interdiscip. Rev.: Comput.*  
21 *Mol. Sci.* **2014**, *4* (1), 15-25.  
22  
23  
24 34. VandeVondele, J.; Hutter, J., *J. Chem. Phys.* **2007**, *127* (11), 114105-114105.  
25  
26  
27 35. Goedecker, S.; Teter, M.; Hutter, J., *Phys. Rev. B* **1996**, *54* (3), 1703-1710.  
28  
29  
30 36. Krack, M., *Theor. Chem. Acc.* **2005**, *114* (1-3), 145-152.  
31  
32  
33 37. Adamo, C.; Barone, V., *J. Chem. Phys.* **1999**, *110* (13), 6158.  
34  
35  
36 38. Ernzerhof, M.; Scuseria, G. E., *J. Chem. Phys.* **1999**, *110* (11), 5029.  
37  
38  
39 39. Guidon, M.; Hutter, J.; VandeVondele, J., *J. Chem. Theory Comput.* **2010**, *6* (8), 2348-2364.  
40  
41  
42 40. Spencer, J.; Alavi, A., *Phys. Rev. B* **2008**, *77* (19), 193110-193110.  
43  
44  
45 41. Pauling, L.; Hendricks, S. B., *J. Am. Chem. Soc.* **1925**, *47*, 781-790.  
46  
47  
48 42. Blake, R. L.; Hessevick, R. E.; Zoltai, T.; Finger, L. W., *Am. Mineral.* **1966**, *51* (1-2), 123-129.  
49  
50  
51 43. Buxton, B. F.; Eades, J. A.; Steeds, J. W.; Rackham, G. M., *Philos. Trans. R. Soc. London, Ser. A*  
52 **1976**, *281* (1301), 171-194.  
53  
54  
55 44. Wills, A. S., *Phys. B (Amsterdam, Neth.)* **2000**, *276*, 680-681.  
56  
57  
58 45. Shull, C. G.; Strauser, W. A.; Wollan, E. O., *Phys. Rev.* **1951**, *83* (2), 333-345.  
59  
60

- 1  
2  
3  
4 46. Capillas, C.; Tasci, E. S.; de la Flor, G.; Orobengoa, D.; Perez-Mato, J. M.; Aroyo, M. I., *Z. Kristallogr.* **2011**, *226* (2), 186-196.  
5  
6  
7  
8 47. Murad, E., *Am. Mineral.* **1982**, *67* (9-10), 1007-1011.  
9  
10  
11 48. Forsyth, J. B.; Hedley, I. G.; Johnson, C. E., *J. Phys. C: Solid State Phys.* **1968**, *1* (1), 179-188.  
12  
13  
14 49. Schmid, H., *J. Phys.: Condens. Matter* **2008**, *20* (43).  
15  
16  
17 50. Perez-Mato, J. M.; Gallego, S. V.; Tasci, E. S.; Elcoro, L.; de la Flor, G.; Aroyo, M. I., *Annu. Rev. Mater. Res.* **2015**, *45*, 217-248.  
18  
19  
20  
21 51. Mandal, P.; Pitcher, M. J.; Alaria, J.; Niu, H. J.; Zanella, M.; Claridge, J. B.; Rosseinsky, M. J., *Adv. Funct. Mater.* **2016**, *26* (15), 2523-2531.  
22  
23  
24  
25 52. Mohamed, M. B.; Senyshyn, A.; Ehrenberg, H.; Fuess, H., *J. Alloys Compd.* **2010**, *492* (1-2), L20-L27.  
26  
27  
28  
29  
30  
31  
32  
33  
34  
35  
36  
37  
38  
39  
40  
41  
42  
43  
44  
45  
46  
47  
48  
49  
50  
51  
52  
53  
54  
55  
56  
57  
58  
59  
60



TOC Graphic

